Springer

Acta Mechanica Sinica

CrossMark click for updates

•RESEARCH PAPER•

Acta Mech. Sin., Vol. 38, 221480 (2022)
https://doi.org/10.1007/s10409-022-09024-x

Comparative study of amorphous and crystalline Zr-based alloys in response to nanosecond pulse laser ablation

Xuan Song[1,2], Xianqian Wu[3], Lanhong Dai[1,2], and Minqiang Jiang[1,2*]

[1] *State Key Laboratory of Nonlinear Mechanics, Institute of Mechanics, Chinese Academy of Sciences, Beijing 100190, China;*
[2] *School of Engineering Science, University of Chinese Academy of Sciences, Beijing 101408, China;*
[3] *Key Laboratory of Mechanics in Fluid Solid Coupling Systems, Institute of Mechanics, Chinese Academy of Sciences, Beijing 100190, China*

Received September 26, 2021; accepted November 30, 2021; published online February 21, 2022

In this work, we comprehensively investigate the response of amorphous and crystalline Zr-based alloys under nanosecond pulse laser ablation. The *in situ* multiphysics processes and ablation morphologies of the two alloy targets are explored and compared. The results indicate that the dynamics of laser-induced plasma and shock waves obey the idea blast wave theory and are insensitive to the topological structures of targets. Both targets experience significant superheating and culminate in explosive boiling. This ablation process leads to the formation of a hierarchical structure in the resultant ablation crater: microdents covered by widespread nanovoids. The amorphous target shows shallower microdents and smaller nanovoids than their crystalline counterparts because the former has a smaller heat-affected zone and experiences a higher degree of superheating. The hierarchical structure can adjust the surface wettability of targets from initial hydrophilic to hydrophobic, showing an increase of the contact angle approximately 119% for amorphous alloy compared with the crystal approximately 64%. This work demonstrates that amorphous alloys have a better performance against nanosecond pulse laser ablation and provides a feasible and one-step method of wettability modification for either amorphous or crystalline alloys.

Amorphous alloys, Nanosecond laser ablation, Plasma, Explosive boiling, Surface wettability

Citation: X. Song, X. Wu, L. Dai, and M. Jiang, Comparative study of amorphous and crystalline Zr-based alloys in response to nanosecond pulse laser ablation, Acta Mech. Sin. **38**, 221480 (2022), https://doi.org/10.1007/s10409-022-09024-x

1. Introduction

Over the past decades, laser technology has shown versatility for amorphous alloys (i.e., metallic glasses) by laser welding [1,2], cladding [3-6], additive manufacturing [7,8], and shock peening [9,10]. Ablation is the fundamental process of laser-solid interaction, accompanied by rapid material removal in the form of plasma, vapor or molten droplets. Laser ablation can thus serve as an effective method in the surface modification, precision micromachining or nanoparticle synthesis of amorphous alloys [11-16], which expands their applications as functional materials. The responses of solids to laser ablation are closely related to both laser parameters and solid properties/structures. In general, the pulse width of the laser can largely affect the ablation mechanisms. This is because the characteristic time required for the laser energy to be converted into heat energy absorbed by solids is on the order of 1 picosecond [17-19]. Therefore, when the pulse width increases from femtosecond to nanosecond or microsecond, laser ablation exhibits an obvious transition from nonthermal to thermal features [20-26]. In addition to normal melting and vaporization, laser-induced plasma and explosive boiling appear with increasing laser intensity during laser thermal ablation. The plasma can further stimulate other concomitant phenomena, including shock waves and cavitation bubbles (if in liquids) [27-29]. These phenomena impose complex perturbations on the molten solid surface, resulting in the formation of various ablation patterns, such as ripples [23], dimples [26], grooves [13], tracks [30], and keyholes [31].

It is commonly believed that a liquid-like disordered

*Corresponding author. E-mail address: mqjiang@imech.ac.cn (Minqiang Jiang)
Executive Editor: Xinglong Gong

structure makes amorphous alloys more susceptible to laser ablation. For example, under femtosecond laser irradiation, it was found that a Zr-based bulk amorphous alloy suffers deeper nonthermal ablation than its crystalline counterpart [32]. The underlying reason is that the amorphous structure has no grain boundaries to excessively dissipate the energy of hot electrons. Under microsecond laser processing, it was observed that an amorphous Ni-based alloy displays a relatively larger melt pool than its crystalline counterpart [21]. This is ascribed to the low thermal conductivity of disordered structures so that more laser energy accumulates on the surface of amorphous alloys. Under nanosecond laser irradiation, however, there is no answer as to whether amorphous alloys undergo more pronounced thermal ablation than their crystalline counterparts. Laser thermal ablation in air usually involves the formation and evolution of plasma and shock waves and violent explosive boiling [25]. The detailed difference of these processes deserves careful investigation between amorphous and crystalline alloys.

In this work, ablation by a nanosecond pulse laser is conducted on a typical Zr-based amorphous alloy and its polycrystalline cousin. We compare the response of two different targets with laser thermal ablation by both *in situ* observations of the ablation process and postmortem characterizations of ablation morphologies. The underlying mechanism is explained based on a thermodynamic model proposed by Jiang et al. [25]. Finally, how the ablation morphologies affect the surface wettability is explored and discussed.

2. Experiment setup

Zr-based amorphous alloys (Vitreloy 1) with a nominal composition $Zr_{41.2}Ti_{13.8}Cu_{12.5}Ni_{10.0}Be_{22.5}$ (at.%) were chosen as the target materials. The as-cast targets were cut into 10 mm × 10 mm square shapes with a thickness of approximately 2 mm. The polycrystalline counterparts were obtained by heating the as-cast targets up to 773 K at a constant heating rate of 5 K/min, followed by isothermal annealing for 2 h and subsequent cooling to room temperature at the same rate. To avoid oxidation, the targets were sealed in a quartz tube filled with pure nitrogen during the above process. Both amorphous and crystalline targets were mechanically ground using SiC papers and polished to a mirror-like appearance with a diamond gel suspension. Single-pulse laser ablation was conducted with a Q-switched Nd:YAG laser operating at a wavelength of 1064 nm and a fixed output energy of approximately 1.9 J per shot. The temporal profile of the laser pulse approximates a Gaussian distribution, and its full width at half maxima (FWHM), i.e., the pulse width, is approximately 10 ns. All ablations were performed in an atmospheric environment and under a normal incident of the laser beam.

An ultrafast camera (Specialised Imaging SIMD) was used to synchronously record the physical processes associated with laser ablation at a frame rate of 10000000 fps. After ablation, the surface morphologies of the targets were examined by using scanning electron microscopy (SEM, GeminiSEM 300) equipped with energy dispersive spectroscopy (EDS), atomic force microscopy (AFM, Veeco DI MultiMode) and optical profilometry (Bruker GT-K). A contact angle meter (Kruss DSA100) was used to evaluate the surface wettability of the targets, and water droplets of 5 μL were selected for measurements. The amorphous or crystalline nature of the targets was confirmed by X-ray diffraction (XRD, Rigaku Smart Lab 9) with Cu K radiation.

3. Results and discussion

3.1 Laser-induced plasma and shock wave

Figure 1a and b show the high spatiotemporal-resolved imaging of the nanosecond laser irradiation of the amorphous and crystalline Vitreloy 1 targets, respectively. Despite their very different topological structures, the two targets exhibit very similar physical processes accompanied by laser ablation. Bright plasma is observed on the target

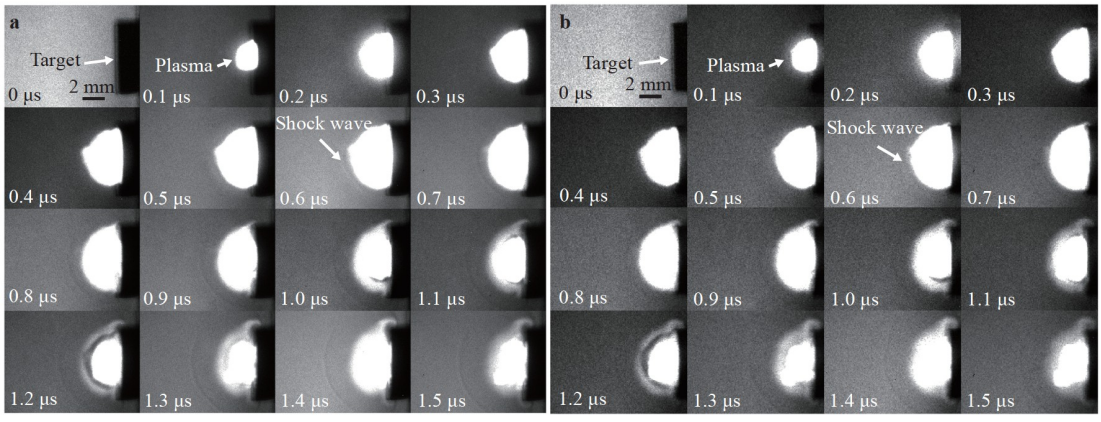

Figure 1 High spatiotemporal-resolved imaging of the ablation process for the **a** amorphous and **b** crystalline targets irradiated by the nanosecond pulse laser.

surface after laser pulse termination, and then it expands rapidly with a hemispherical shape and reaches the maximum size at approximately 600 ns. At the same time, a shock wave is visible to separate from the plasma front edge, as indicated by the arrows in Figure 1. After that, the shock wave continues to expand, while the plasma begins to attenuate. The attenuation of plasma is manifested as an obvious dimming from the edge in the time range of 0.8-1.2 μs. Another light emission with a hemisphere shape can be observed inside the attenuated plasma at approximately 1.0 μs. This light emission is attributed to the violent ejection of ablated material, which is composed of high-temperature vapor and droplets. It is well accepted that the instantaneous ejection of ablation matter provides convincing evidence for the explosive boiling of the superheated liquid. In fact, the occurrence of explosive boiling can be traced back to tens of nanoseconds after laser pulse termination [25,33,34], but here, it is obscured by plasma emission before 1.0 μs. The matter ejection quickly expands outward with an explosive feature after 1.2 μs. The observed ablation process is schematically illustrated in Figure 2.

We further measure the propagation dynamics of laser-induced plasma and shock waves in the current time window (1.5 μs), as presented in Fig. 3, where the largest distance D from their front edge to the target surface is plotted as a function of time t. Consistent with the direct observations in Fig. 1, the amorphous and crystalline targets have almost the same dynamics of plasma and shock waves. Except for a slight discontinuity at the moment (600 ns) when the shock wave separates from the plasma, their dynamics can be solely fitted by the power law: $D \sim t^{0.448}$. The decay rate (0.448) is close to that (0.4) of ideal blast wave theory for a spherical wave [33,35]. This implies that all energy is instantaneously released by a point source and that the shock is strong enough to neglect the ambient pressure. Vorob'ev et al. [36] proposed a numerical expression to estimate the velocity of laser-supported detonation waves in air:

$$v_{\mathrm{LSDW}} \approx 8.48(I/P)^{1/3}, \tag{1}$$

where I is the incident laser intensity, normalized by 100 MW/cm^2, and P is the ambient gas pressure, normalized by 1 atm. Under the current conditions, the laser intensity I is estimated to be approximately 2.2 GW/cm^2, obtained by the ratio of the pulse laser power to the real area of the ablation crater (see Fig. 4). This intensity ensures the occurrence of explosive boiling for the Vitreloy 1 targets in the air environment [25]. Then, we have the normalized $I \approx 22.4$ and the normalized $P=1$. Thus, v_{LSDW} is calculated to be approximately 24 km/s. From the measurement in Fig. 3, we find that in the initial 100 ns, the plasma propagates for approximately 2.3 mm, which corresponds to an averaged velocity V of approximately 23 km/s. Such agreement implies that the initiation of the hypersonic-velocity plasma or shock wave can be regarded as a detonation wave induced by a high-energy laser. This is different from that of underwater laser ablation, where the initial shock wave is a planar detonation wave due to the strong confinement of water [29].

Furthermore, based on the calculated or measured V, the initial pressure of the shock wave can be calculated as [37]:

$$P = \rho V \frac{V-c}{1.99}\ (\mathrm{GPa}), \tag{2}$$

where c and ρ denote the acoustic velocity (0.34 km/s) and density (1.293 g/cm^3) of the ambient air, respectively. The initial pressure of the shock wave is calculated to be approximately 339 MPa. This value is close to the theoretical result of plasma pressure under similar conditions [38], which confirms that the plasma excites shock waves by momentum transfer. Such a momentum balance mechanism is also satisfied for underwater nanosecond laser ablation [29], although in the latter, the pressure value is much higher than that of in-air ablations with the same conditions. We must note that another compressive wave is simultaneously excited by the plasma and propagates inward to the target, as illustrated in Fig. 2. The two shock waves have the same peak pressure as the plasma at the critical moment of their

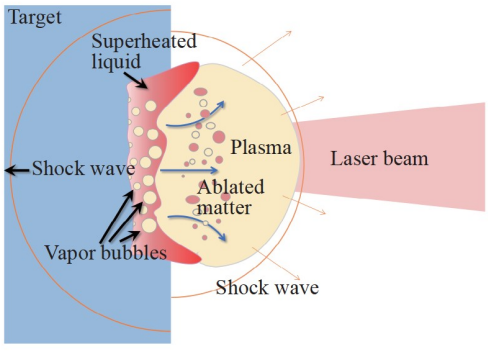

Figure 2 A schematic illustration of the physical phenomena that occurred during nanosecond laser ablation of the solid target.

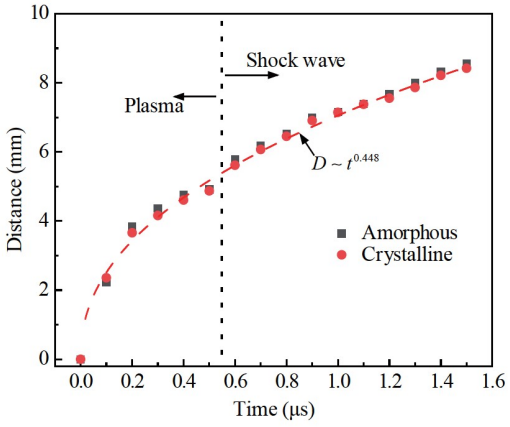

Figure 3 Propagation distances versus time of the plasma and shock wave from the target surfaces of the amorphous (black squares) and crystalline (red circles) targets. The dashed line is the best-fitting result with the power law: $D \sim t^{0.448}$.

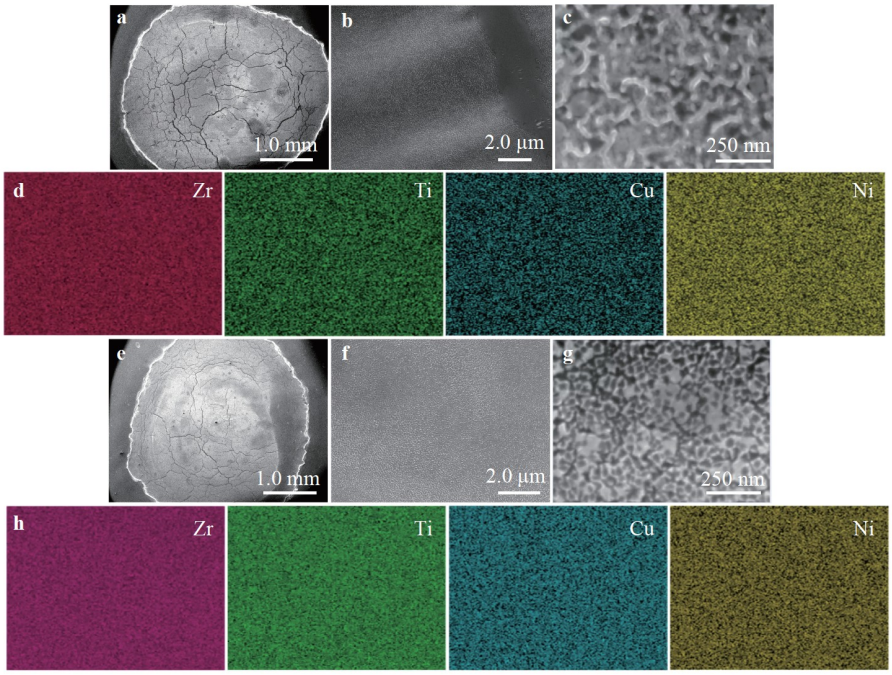

Figure 4 SEM/EDS results of the ablation morphologies for the **a-d** amorphous and **e-h** crystalline targets. **a**, **e** Full view of the ablation craters. **b**, **c** and **f-g** Porous nanostructures at different magnifications. **d**, **h** EDS element mapping corresponding to areas **c** and **g**, respectively.

formation [29]. The above results indicate that the laser-induced plasma and shock wave are less related to the atomic packing configuration of targets. A previous study focused on the plasma behavior of conventional crystals (Cu, Al, and stainless steel) also showed that the plasma dynamics were insensitive to the target materials but highly dependent on the laser parameters [39]. It is noted that the pressure of the inward shock wave is much smaller than the Hugoniot elastic limit of the two targets [40]. Therefore, under the present laser conditions, thermal ablation is the dominant damage of target surfaces.

3.2 Ablation morphology

Figure 4 presents the SEM results of the ablation morphology for the amorphous and crystalline targets. The ablation craters of the two targets have similar shapes and sizes, which are determined by the laser spots, as shown in Fig. 4a and e. The entire ablation crater involves a relatively flat inner region and a ripple edge. The surface ripple formation is ascribed to the Kelvin-Helmholtz hydrodynamic instability occurring at the interface between the molten layer and the expanding plasma, which has been quantitatively described in our previous work [23]. Enlarged views of the inner regions of the two targets are displayed in Fig. 4b, c and f, g. A porous nanostructure is widely distributed in seemingly flat inner areas. The nanovoid morphology is generally considered to be one of the typical characteristics of explosive boiling, which corresponds to the loci where vapor bubbles nucleate and grow in the superheated liquid. Figure 4c and g compare the nanovoid morphology of the amorphous and crystalline targets. At the same scale, there exists a general difference in the nanovoid size. Furthermore, Fig. 4d and h show the EDS element mappings measured from the region in Fig. 4c and g, respectively. The elements Zr, Ti, Cu, and Ni are distributed uniformly in the porous region, indicating that the formation of nanostructures is not accompanied by the segregation of constituent elements. The crack-like patterns in Fig. 4a and e are due to the solidification of some residual superheated liquid that is not completely ablated by explosive boiling.

Table 1 gives the quantitative results of element composition inside and outside the craters of the amorphous and crystalline targets. In addition to the four elements mentioned above, O is present, but the lightest element Be cannot be detected by EDS. We find that the present laser ablation does not change the original composition of targets significantly. The involvement of O stems from the air environment, and the exterior of the ablation crater contains more oxygen than the interior. This can be explained by the shielding effect of the plasma or vapor, which suppresses the direct contact between the high-temperature molten pool and air. The glass natures of the two targets are verified by the XRD patterns before and after ablation, as shown in Fig. 5.

Table 1 Element compositions inside and outside the ablation craters of the amorphous and crystalline targets

Target		Element (at%)				
		Zr	Ti	Cu	Ni	O
Amorphous	Inside	51.98	14.97	15.16	11.96	5.93
	Outside	49.42	14.39	15.77	12.31	8.12
Crystalline	Inside	53.41	15.58	15.69	10.81	4.51
	Outside	50.67	15.31	15.37	11.59	7.06

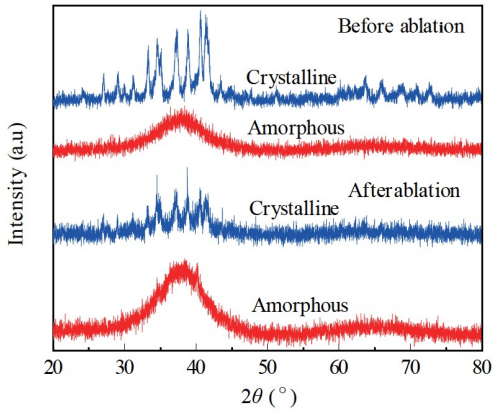

Figure 5 XRD patterns of the ablation craters for the amorphous and crystalline targets before and after laser ablation.

The amorphous target shows typical diffuse scattering peaks before ablation, and laser ablation does not introduce obvious crystallization. For the crystalline counterpart, the target shows a tendency from multiple crystallization peaks to diffuse scattering peaks.

Figure 6 shows the surface contours of the ablation craters for the amorphous and crystalline targets, including the flat inner region (Fig. 6b-e) and the ripple edge (Fig. 6a, c, d, f). The edge ripples are distributed symmetrically about the center and cover a width of approximately 200 μm. Most of the edge ripples are higher than the datum plane and have a height value in the range of 10-20 μm. A sunken circle area is closely adjacent to the ripples and has a width of approximately 200 μm and a depth of approximately 10 μm. The distinct height variation between the raised ripples and sunken circle means that the molten material has a severe flow and redeposition on the crater edge. The inner region is mainly composed of slight dents with depths of less than 1 μm, as shown in Fig. 6b and e. Some protuberances and grooves are distributed on the micron dents, and their height variation is in the range of ±5 μm. The results in Fig. 6 show that the ablation craters of the two targets have almost the same characteristics. Nevertheless, these ablation features display the size difference on the micron scale: the maximum depth of the crystalline target in different regions is generally larger than that of the amorphous target.

Combining Figs. 4 with 6, we confirm that nanosecond laser thermal ablation produces hierarchical micro/nanostructural craters, namely, microdents covered by nanovoids, via explosive boiling. This kind of ablation morphology is clearly different from conventional molten-induced craters. For the latter, the crater has the maximum depth at its center and becomes gradually shallow toward the edge [13,21,30]. Next, the possible mechanism of the observed hierarchical structure is briefly explained. When the target is irradiated by the laser, the laser energy will turn into heat on picosecond time scales and lead to a temperature rise [17]. Under the current conditions, the target is rapidly superheated beyond its boiling point and enters a metastable liquid state. When the temperature approaches the thermodynamic critical point, the superheated liquid beaks down into a mixture of droplets and vapor; see Fig. 2. The violent ejection of abla-

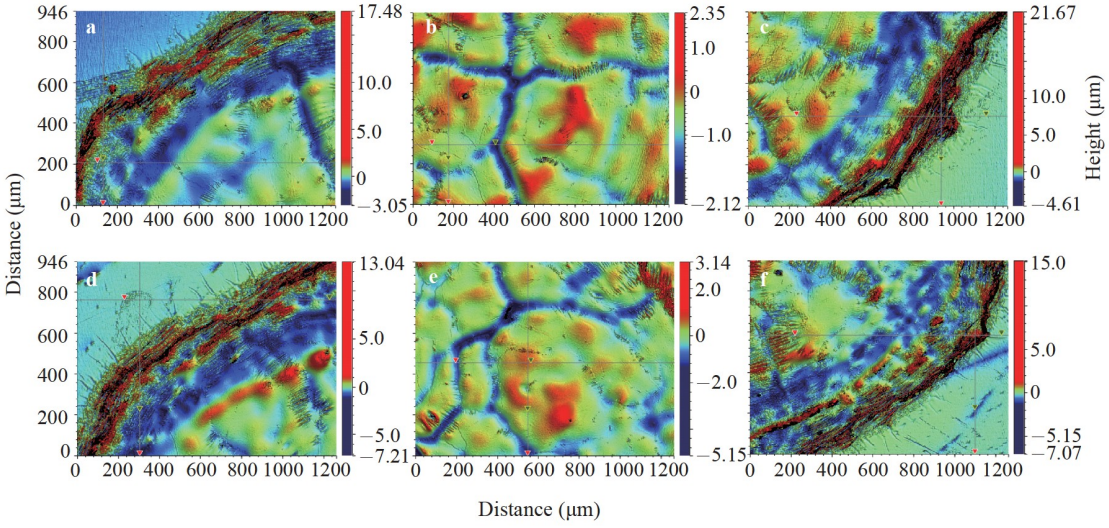

Figure 6 Surface contours of the ablation craters for the **a-c** amorphous and **d-f** crystalline targets.

tion materials leaves the microdents on the target surface. Meanwhile, vapor bubbles nucleate and grow within the superheated liquid, and nanovoids are formed when the residual liquid is solidified [25].

The SEM observations in Fig. 4 indicate that the two targets have a significant size difference in the nanovoids. A more precise scan for these nanostructures is performed by AFM, as shown in Fig. 7. Figure 7a and b present the 3D morphologies for the nanovoids of two targets, and the characterized area is 5 μm × 5 μm. The frequency of the crystalline target at the height extremum is higher than that of the amorphous target. Figure 7c gives the surface profiles along the white lines in the 3D map of Fig. 7a and b. The widths of the porous nanostructure are approximately 100 nm, and most of their depths do not exceed 30 nm. By comparison, we find that the height fluctuation of the crystalline material is obviously more severe than that of the amorphous material. The statistical results of the height values obtained from the whole 3D map are given in Fig. 7d and e. Obviously, the crystalline target has a larger extreme value and a wider distribution of the height values than the amorphous target. The minimum depths are approximately −17 nm and −30 nm for the amorphous and crystalline targets, respectively. More than 90% of the heights are distributed in the range of (−10, 10) nm for the amorphous target and (−20, 20) nm for the crystalline target. This means that the nanovoids of amorphous materials are generally smaller, but their number is greater than that of crystalline materials.

3.3 Mechanism of laser thermal ablation

Based on the multiscale observations of the ablation craters mentioned above, we know that the amorphous and crystalline targets show similar ablation features on different length scales, such as ripples, dents, grooves, and nanovoids. However, compared with the crystalline targets, the amorphous targets exhibit relatively shallower microdents and smaller nanovoids. It is well known that the ablation morphology under a nanosecond pulse laser depends on the thermodynamic processes experienced by the target. To explain the size difference in ablation features of two targets, we calculate the time-dependent temperature $T(x, t)$ along the target depth by the 1D heat convection-diffusion equation [25,41]:

$$\rho C_p\left[\frac{\partial T(x,t)}{\partial t}-\frac{\partial x}{\partial t}\Big|_{x=0}\frac{\partial T}{\partial x}\right] = K\frac{\partial^2 T(x,t)}{\partial x^2}+\alpha[1-R(T_s)]I(t)\mathrm{e}^{-\alpha x}, \tag{3}$$

where ρ, C_p, K and α are the density, heat capacity, thermal conductivity and absorption coefficient of the target, re-

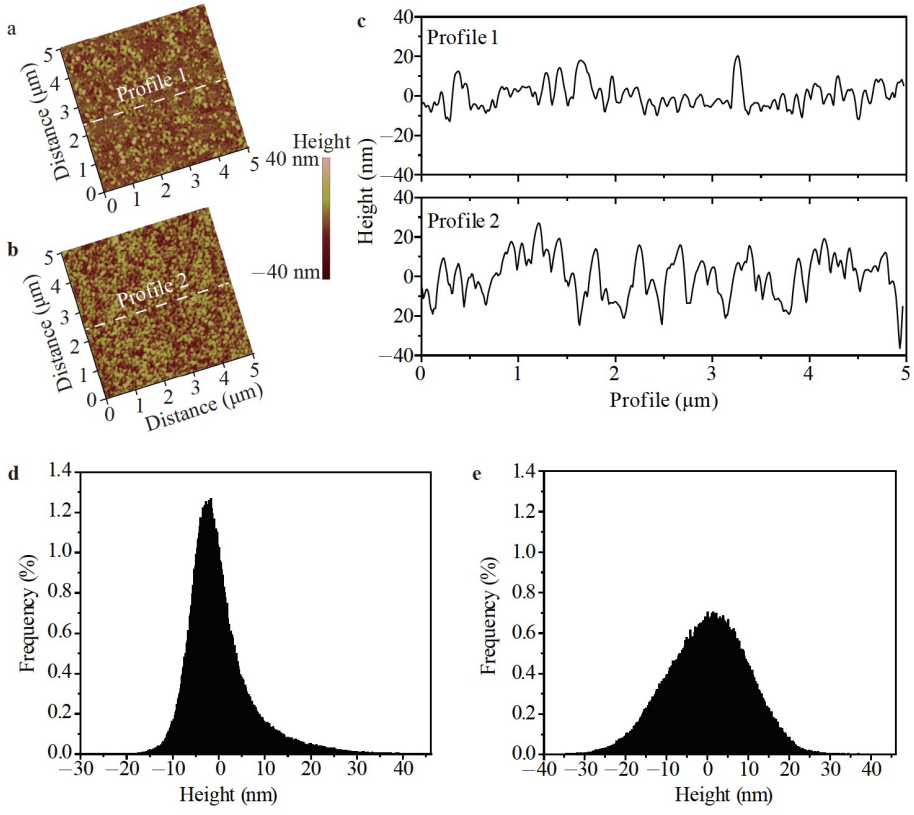

Figure 7 AFM patterns of the nanovoid structures for the **a** amorphous and **b** crystalline targets. **c** Surface profiles along the white lines in **a** and **b**. **d**, **e** The statistical values of the heights from the whole 3D patterns in **a** and **b**, respectively.

spectively, and $R(T_s)$ is the reflectivity of the laser pulse by the target surface, which is a function of the surface temperature $T_s = T(0,t)$. A detailed description for each item in Eq. (3) can refer to our previous work [25]. This partial differential equation is solved by the finite difference method. The surface vapor pressure p_s can be further calculated according to T_s by the modified Clausius-Clapeyron equation. The relevant physical or material parameters used in calculations come from Refs. [25,42] and are listed in Table 2, where the thermal conductivity is significantly different for the two targets.

Figure 8a shows the calculated temperature profiles $T(x, t)$ within the two targets at different times. We can see that the target surface always undergoes the maximum temperature rise, and the temperature at each time decreases from the surface toward the inside. This result confirms one more time that explosive boiling rather than subsurface superheating is the only physically sound mechanism for the nanosecond laser thermal ablation of metal targets, either amorphous or crystalline. We also note that the surface depth that can reach the boiling point (T_b=3792 K) is approximately 0.5 μm,close to the depth of the microdents in Fig. 6. This means that the superheated liquid beyond T_b participates in violent ejection via explosive boiling. In addition, the region affected by high temperature within the crystalline target is slightly deeper than that of the amorphous target. Such a size difference at the microscale is also consistent with the experimental observation of the crater depth in Fig. 6. In fact, grain boundaries in crystals serve as a fast diffusion path facilitating the transport of heat. The absence of grain boundaries in amorphous alloys is not conducive to heat transfer, so the heat is prone to accumulation at shorter distances below the target surface. Therefore, the amorphous target has a higher surface temperature but a shallower heat-affected zone than its crystalline counterpart.

Table 2 The relevant parameters of the targets and the nanosecond laser used

Parameters	Notation	Value/expression
Density of target	ρ	6125 kg m^{-3}
Heat capacity of target	Cp	420 J kg^{-1} K^{-1}
Thermal conductivity of amorphous target	K_a	4.8 Wm^{-1} K^{-1}
Thermal conductivity of crystalline target	K_c	9 Wm^{-1} K^{-1}
Absorption coefficient	α	0.01 nm^{-1}
Reflectivity	R	$R(T_s)$
Laser intensity	I_0	2.2 GW cm^{-2}
Laser fluence	E_0	22 J cm^{-2}
Adjustable coefficients	a	10^7 cm^{-1}
	b	1 cm^2 J^{-1}
Absorbed fluence	E_a	$0.3E_0$
Vaporization coefficient	δ	0.82
Molar mass	M	60 g mol^{-1}
Latent heat	L	438 kJ mol^{-1}
Boiling point	T_b	3792 K
TCP	T_c	7196 K
Reduction coefficient	$\xi(T_s)$	ξ=(5−2T_s/T_b)/3
Density of superheated liquid	ρ_l	6020 kg m^{-3}
Density of vapor	ρ_v	(10^{-2}-10^{-3})ρ_l

Figure 8b shows the surface temperature T_s and vapor pressure p_s of the two targets. The target surface is rapidly superheated above T_b within a pulse width of 10 ns. Explosive boiling usually initiates at the peak temperature T_l of the superheated liquid. This temperature T_l is 6685 K at 19 ns for the amorphous target and 6239 K at 24 ns for the crystalline target. During the heating process, the surface vapor pressure also rapidly increases from the standard atmospheric pressure p_b to the maximum p_l of approximately 190 p_b and 134 p_b for the amorphous and crystalline targets, respectively. Compared with the crystalline target, the amorphous target experiences a higher degree of superheating and explosive boiling but at an earlier time.

It has been revealed that the nanovoids in the ablation crater result from the spontaneous nucleation of vapor bubbles within the superheated liquid. The critical radius that bubbles can nucleate is evaluated as [25]:

$$r_c = \tau_c \sqrt{\frac{3\rho_l T_{\mathrm{sat}}(p_l)}{2L\rho_v[T_l - T_{\mathrm{sat}}(p_l)]}}, \tag{4}$$

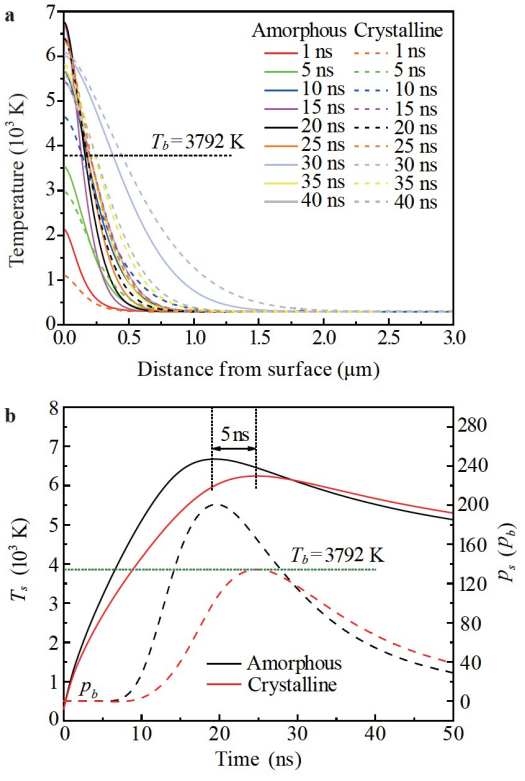

Figure 8 Calculated time evolution of **a** the temperature profiles within the amorphous and crystalline targets and **b** the surface temperature and vapor pressure.

where ρ_l and ρ_v are the densities of superheated liquid and vapor, L is the latent heat of evaporation, T_l and p_l are the peak surface temperature and pressure of the superheated liquid, and T_{sat} is the saturation temperature that links p_l by the Clausius-Clapeyron equation. The critical time of nucleation τ_c is defined as the time lag between normal boiling and explosive boiling, which can be determined from Fig. 8b. Thus, r_c is calculated to be approximately 5 nm and 9 nm for the amorphous and crystalline targets, respectively. The calculated r_c is approximately 1/3 of the AFM measurements (~15 nm and ~30 nm in Fig. 7). Such a size gap should result from the further growth of the nucleated bubble into the observed nanovoids. The relatively smaller r_c for the amorphous target is consistent with the higher degree of superheating and more violent explosive boiling (Fig. 8). This is because increasing T_l corresponds to an increase in p_l, which leads to a decrease in r_c.

3.4 Surface wettability

Finally, it is interesting to study the surface wettability of the micro/nanostructures induced by laser ablation [14-16], which in turn is helpful for understanding the ablation mechanism. Before ablation, the polished surface of the amorphous target shows a contact angle of approximately 53°, while 72° for the crystalline counterpart, as shown in Fig. 9a. Obviously, the initial surface of Vitreloy 1 alloys is hydrophilic. After ablation, both amorphous and crystalline targets show an enhanced contact angle of approximately 117°±1°, as shown in Fig. 9b. Such hydrophobic behavior should be due to the hierarchical ablation morphologies, as shown in Figs. 4, 6 and 7.

Usually, there are two factors affecting the contact angle, that is, the surface free energy (SFE) γ and the surface topological morphologies. We first consider the contact situation before ablation, as illustrated in Fig. 9c. Here, the surface morphologies mainly result from the toughness of the polished surface. The contact angle can be described by a toughness-modified Young's equation [43], i.e., the so-called Wenzel model [44]:

$$\cos\theta^* = R_f \cos\theta^i = R_f \frac{\gamma_{sg} - \gamma_{ls}}{\gamma_{lg}}, \tag{5}$$

where θ^* and θ^i are the apparent and intrinsic contact angles, respectively, and R_f is the surface roughness factor defined as the ratio between the actual and projected areas. The subscripts s, g and l represent solid, gas and liquid, respectively. Before ablation, the values R_f are comparable for both amorphous and crystalline surfaces by careful polishing. The value of γ_{lg} is determined by the liquid droplet and atmospheric environment, which can be regarded as constant. Amorphous alloys reside in thermodynamically metastable states where the dynamics of atoms are highly active, especially near the surface [45,46]. Therefore, their SFE γ_{sg} is higher than that of the crystalline target. On the other hand, increasing γ_{sg} will enhance the attraction between the liquid molecules and the solid atoms, facilitating the spreading of the liquid drop on the target surface, thus decreasing γ_{ls} [47]. Therefore, according to Eq. (5), the equilibrium contact angle of amorphous alloys is theoretically smaller than that of their crystalline counterparts. This agrees with the experimental measurements in Fig. 9a.

We further consider the contact situation after ablation, as illustrated in Fig. 9d. Here, the surface morphologies become hierarchical micro/nanostructures, which change the interface of the droplet-target from full to partial contact. Thus, the real interface can be regarded as a composite of solid-liquid-gas. The contact angle θ of this composite surface is described by the Cassie-Baxter model [48]:

$$\cos\theta = f_1 \cos\theta_1 + f_2 \cos\theta_2, \tag{6}$$

where subscript 1 denotes the solid target, subscript 2 denotes air, and f_1 and f_2 are their respective fractions occupying the whole surface area, which satisfies $f_1 + f_2 = 1$. The

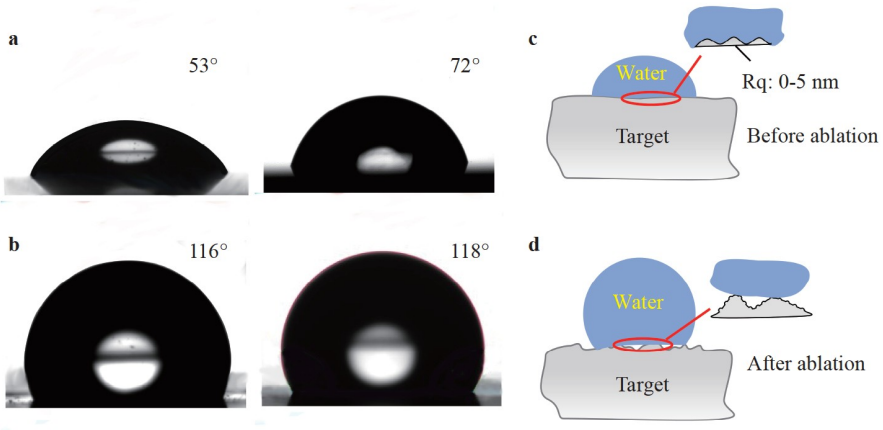

Figure 9 Surface contact angles for the amorphous and crystalline targets **a** before and **b** after laser ablation. Schematic illustration of the contact situations between the water droplet and target surface **c** before and **d** after laser ablation.

contact angle θ_2 of air to water is 180°, and θ= 117° according to Fig. 9b. Thus, we obtain the relation

$$(1+\cos\theta_1)f_1 = 0.546, \tag{7}$$

which satisfies both amorphous and crystalline targets. From Fig. 9a, the contact angles θ_1 for the two targets are 53° and 72°. Therefore, we can further obtain a relation about the solid-water contact area f_1 for the two targets, which reads

$$\frac{(f_1)_{\text{amor}}}{(f_1)_{\text{cryst}}} = 0.817. \tag{8}$$

This relation indicates that for the amorphous target, the solid area fraction in the ablation crater is only approximately 81.7% of that of the crystalline material. This analysis agrees well with the results in Fig. 7, where the amorphous target indeed shows a larger number of nanovoids with relatively smaller sizes. Such removal of more solid matter is also well explained by the higher degree of superheating and explosive boiling, as shown in Fig. 8.

4. Conclusions

The ablations of an amorphous Vitreloy 1 alloy and its crystalline counterpart are comprehensively studied under a nanosecond pulse laser in air. By comparison, we can derive important conclusions as follows.

(1) Despite very different topological structures, the two alloys share similar dynamics for laser-induced plasma and shock waves. The rapidly expanding plasma excites the shock wave propagating into air, which is dominated by momentum transfer.

(2) Both alloys suffer significant thermal ablation in the form of explosive boiling, which incurs an ablation crater with a hierarchical morphology: microdents covered by nanovoids. Compared with crystalline alloys, the ablation crater of amorphous alloys is of relatively shallower depth but consists of a larger number of nanovoids with smaller sizes.

(3) The morphologies of ablation craters are further explained by theoretical analyses. The underlying mechanism is that the amorphous alloy target experiences a higher degree of surface superheating and explosive boiling but has a relatively smaller heat-affected zone than the crystalline target. In other words, for amorphous alloys, significant explosive boiling is confined within a relatively shallower ablation depth, thus showing a better performance against nanosecond pulse laser ablation.

(4) The present laser thermal ablation provides a feasible way to modify the surface wettability of alloys, either amorphous or crystalline. The initially hydrophilic surface can become hydrophobic due to the ablation-induced hierarchical surface morphologies. The amorphous target shows a more obvious increase in the surface contact angle, which is ascribed to a substantial amount of matter removal via highly violent explosive boiling.

This work was supported by the National Outstanding Youth Science Fund Project (Grant No. 12125206) of the National Natural Science Foundation of China (NSFC), the NSFC Basic Science Center for "Multiscale Problems in Nonlinear Mechanics" (Grant No. 11988102), and the NSFC (Grant Nos. 11972345 and 11790292).

1 J. Kim, D. Lee, S. Shin, and C. Lee, Phase evolution in $Cu_{54}Ni_6Zr_{22}$-Ti_{18} bulk metallic glass Nd:YAG laser weld, Mater. Sci. Eng.-A **434**, 194 (2006).
2 G. Wang, Y. J. Huang, M. Shagiev, and J. Shen, Laser welding of $Ti_{40}Zr_{25}Ni_3Cu_{12}Be_{20}$ bulk metallic glass, Mater. Sci. Eng.-A **541**, 33 (2012).
3 D. T. A. Matthews, V. Ocelík, and J. T. M. de Hosson, Scratch test induced shear banding in high power laser remelted metallic glass layers, J. Mater. Res. **22**, 460 (2007).
4 D. T. A. Matthews, V. Ocelík, and J. T. M. de Hosson, Tribological and mechanical properties of high power laser surface-treated metallic glasses, Mater. Sci. Eng.-A **471**, 155 (2007).
5 H. Sun, and K. M. Flores, Microstructural analysis of a laser-processed Zr-based bulk metallic glass, Metall. Mat. Trans. A **41**, 1752 (2010).
6 H. Sun, and K. M. Flores, Spherulitic crystallization mechanism of a Zr-based bulk metallic glass during laser processing, Intermetallics **43**, 53 (2013).
7 Y. Shen, Y. Li, C. Chen, and H. L. Tsai, 3D printing of large, complex metallic glass structures, Mater. Des. **117**, 213 (2017).
8 S. Pauly, L. Löber, R. Petters, M. Stoica, S. Scudino, U. Kühn, and J. Eckert, Processing metallic glasses by selective laser melting, Mater. Today **16**, 37 (2013).
9 Y. Li, K. Zhang, Y. Wang, W. Tang, Y. Zhang, B. Wei, and Z. Hu, Abnormal softening of Ti-metallic glasses during nanosecond laser shock peening, Mater. Sci. Eng.-A **773**, 138844 (2020).
10 J. Fu, Y. Zhu, C. Zheng, R. Liu, and Z. Ji, Effect of laser shock peening on mechanical properties of Zr-based bulk metallic glass, Appl. Surf. Sci. **313**, 692 (2014).
11 H. Huang, M. Jiang, and J. Yan, The coupling effects of laser thermal shock and surface nitridation on mechanical properties of Zr-based metallic glass, J. Alloys Compd. **770**, 864 (2019).
12 X. Song, K. L. Xiao, X. Q. Wu, G. Wilde, and M. Q. Jiang, Nanoparticles produced by nanosecond pulse laser ablation of a metallic glass in water, J. Non-Crystalline Solids **517**, 119 (2019).
13 Y. Jiao, E. Brousseau, X. Shen, X. Wang, Q. Han, H. Zhu, S. Bigot, and W. He, Investigations in the fabrication of surface patterns for wettability modification on a Zr-based bulk metallic glass by nanosecond laser surface texturing, J. Mater. Process. Tech. **283**, 116714 (2020).
14 Y. Qian, M. Jiang, Z. Zhang, H. Huang, and J. Yan, On the transformation between micro-concave and micro-convex in nanosecond laser ablation of a Zr-based metallic glass, J. Manufact. Processes **68**, 1114 (2021).
15 M. V. Rukosuyev, J. Lee, S. J. Cho, G. Lim, and M. B. G. Jun, One-step fabrication of superhydrophobic hierarchical structures by femtosecond laser ablation, Appl. Surf. Sci. **313**, 411 (2014).
16 J. Long, Z. He, C. Zhou, X. Xie, Z. Cao, P. Zhou, Y. Zhu, W. Hong, and Z. Zhou, Hierarchical micro- and nanostructures induced by nanosecond laser on copper for superhydrophobicity, ultralow water adhesion and frost resistance, Mater. Des. **155**, 185 (2018).
17 B. N. Chichkov, C. Momma, S. Nolte, F. Alvensleben, and A. Tünnermann, Femtosecond, picosecond and nanosecond laser ablation of solids, Appl. Phys. A **63**, 109 (1996).
18 X. Y. Wang, D. M. Riffe, Y. S. Lee, and M. C. Downer, Time-resolved electron-temperature measurement in a highly excited gold

target using femtosecond thermionic emission, Phys. Rev. B **50**, 8016 (1994).
19 R. W. Schoenlein, W. Z. Lin, J. G. Fujimoto, and G. L. Eesley, Femtosecond studies of nonequilibrium electronic processes in metals, Phys. Rev. Lett. **58**, 1680 (1987).
20 W. Jia, Z. Peng, Z. Wang, X. Ni, and C. Wang, The effect of femtosecond laser micromachining on the surface characteristics and subsurface microstructure of amorphous FeCuNbSiB alloy, Appl. Surf. Sci. **253**, 1299 (2006).
21 I. Quintana, T. Dobrev, A. Aranzabe, G. Lalev, and S. Dimov, Investigation of amorphous and crystalline Ni alloys response to machining with micro-second and pico-second lasers, Appl. Surf. Sci. **255**, 6641 (2009).
22 F. Ma, J. Yang, J. XiaonongZhu, C. Liang, and H. Wang, Femtosecond laser-induced concentric ring microstructures on Zr-based metallic glass, Appl. Surf. Sci. **256**, 3653 (2010).
23 Y. Liu, M. Q. Jiang, G. W. Yang, Y. J. Guan, and L. H. Dai, Surface rippling on bulk metallic glass under nanosecond pulse laser ablation, Appl. Phys. Lett. **99**, 191902 (2011).
24 W. Zhang, G. Cheng, X. D. Hui, and Q. Feng, Abnormal ripple patterns with enhanced regularity and continuity in a bulk metallic glass induced by femtosecond laser irradiation, Appl. Phys. A **115**, 1451 (2013).
25 M. Q. Jiang, Y. P. Wei, G. Wilde, and L. H. Dai, Explosive boiling of a metallic glass superheated by nanosecond pulse laser ablation, Appl. Phys. Lett. **106**, 021904 (2015).
26 E. Williams, and E. B. Brousseau, Nanosecond laser processing of $Zr_{41.2}Ti_{13.8}Cu_{12.5}Ni_{10}Be_{22.5}$ with single pulses, J. Mater. Process. Tech. **232**, 34 (2016).
27 M. Q. Jiang, X. Q. Wu, Y. P. Wei, G. Wilde, and L. H. Dai, Cavitation bubble dynamics during pulsed laser ablation of a metallic glass in water, Extreme Mech. Lett. **11**, 24 (2017).
28 T. T. P. Nguyen, R. Tanabe, and Y. Ito, Comparative study of the expansion dynamics of laser-driven plasma and shock wave in in-air and underwater ablation regimes, Opt. Laser Tech. **100**, 21 (2018).
29 X. Song, X. Q. Wu, K. L. Xiao, C. Li, H. Y. Wang, and M. Q. Jiang, Nanosecond laser ablation of a metallic glass in water: a high time-resolved imaging study, Philos. Mag. **100**, 2708 (2020).
30 H. Huang, N. Jun, M. Jiang, M. Ryoko, and J. Yan, Nanosecond pulsed laser irradiation induced hierarchical micro/nanostructures on Zr-based metallic glass substrate, Mater. Des. **109**, 153 (2016).
31 C. Zhao, Q. L. Guo, X. X. Li, N. Parab, K. Fezzaa, W. Tan, L. Chen, and T. Sun. Bulk-explosion-induced metal spattering during laser processing, Phys. Rev. X **9**, 021052 (2019).
32 T. Sano, K. Takahashi, A. Hirose, and K. F. Kobayashi, Femtosecond laser ablation of $Zr_{55}Al_{10}Ni_5Cu_{30}$ bulk metallic glass, Mater. Sci. Forum **539**, 1951 (2007).
33 S. S. Harilal, G. V. Miloshevsky, P. K. Diwakar, N. L. LaHaye, and A. Hassanein, Experimental and computational study of complex shockwave dynamics in laser ablation plumes in argon atmosphere, Phys. Plasmas **19**, 083504 (2012).
34 X. Xu, Phase explosion and its time lag in nanosecond laser ablation, Appl. Surf. Sci. **197-198**, 61 (2002).
35 S. H. Jeong, R. Greif, and R. E. Russo, Propagation of the shock wave generated from excimer laser heating of aluminum targets in comparison with ideal blast wave theory, Appl. Surf. Sci. **127-129**, 1029 (1998).
36 V. A. Vorob'ev, M. F. Kanevskii, and S. Y. Chernov, Investigation of the dynamics of a laser-supported detonation wave using a self-consistent numerical model, J. Soviet Laser Res. **12**, 269 (1991).
37 T. Pezeril, G. Saini, D. Veysset, S. Kooi, P. Fidkowski, R. Radovitzky, and K. A. Nelson, Direct visualization of laser-driven focusing shock waves, Phys. Rev. Lett. **106**, 214503 (2011).
38 D. Marla, Y. Zhang, J. H. Hattel, and J. Spangenberg, Modeling of nanosecond pulsed laser processing of polymers in air and water, Model. Simul. Mater. Sci. Eng. **26**, 055005 (2018).
39 J. Wu, W. Wei, X. Li, S. Jia, and A. Qiu, Infrared nanosecond laser-metal ablation in atmosphere: Initial plasma during laser pulse and further expansion, Appl. Phys. Lett. **102**, 164104 (2013).
40 G. Ding, C. Li, A. Zaccone, W. H. Wang, H. C. Lei, F. Jiang, Z. Ling, and M. Q. Jiang, Ultrafast extreme rejuvenation of metallic glasses by shock compression, Sci. Adv. **5**, eaaw6249 (2019).
41 N. M. Bulgakova, and A. V. Bulgakov, Pulsed laser ablation of solids: transition from normal vaporization to phase explosion, Appl Phys A **73**, 199 (2001).
42 M. Yamasaki, S. Kagao, Y. Kawamura, and K. Yoshimura, Thermal diffusivity and conductivity of supercooled liquid in $Zr_{41}Ti_{14}Cu_{12}Ni_{10}Be_{23}$ metallic glass, Appl. Phys. Lett. **84**, 4653 (2004).
43 T. Young, An essay on the cohesion of fluids, Phil. Trans. R. Soc. **95**, 65 (1805).
44 R. N. Wenzel, Resistance of solid surfaces to wetting by water, Ind. Eng. Chem. **28**, 988 (1936).
45 J. Ma, C. Yang, X. Liu, B. Shang, Q. He, F. Li, T. Wang, D. Wei, X. Liang, X. Wu, Y. Wang, F. Gong, P. Guan, W. Wang, and Y. Yang, Fast surface dynamics enabled cold joining of metallic glasses, Sci. Adv. **5**, eaax7256 (2019).
46 N. Chen, D. Wang, P. F. Guan, H. Y. Bai, W. H. Wang, Z. J. Zhang, H. Hahn, and H. Gleiter, Direct observation of fast surface dynamics in sub-10-nm nanoglass particles, Appl. Phys. Lett. **114**, 043103 (2019).
47 G. F. Ma, H. F. Zhang, H. Li, and Z. Q. Hu, Influence of structural relaxation on wetting behavior of molten In-Sn alloy on $Cu_{40}Zr_{44}Al_8Ag_8$ bulk metallic glass, J. Alloys Compd. **513**, 273 (2012).
48 A. B. D. Cassie, and S. Baxter, Wettability of porous surfaces, Trans. Faraday Soc. **40**, 0546 (1944).

非晶态与晶态锆基合金对纳秒脉冲激光烧蚀响应的对比研究

宋璇, 吴先前, 戴兰宏, 蒋敏强

摘要 本文系统性地对比研究了非晶态与晶态锆基合金对纳秒脉冲激光的烧蚀响应，主要关注两种合金靶的多物理烧蚀过程以及靶表面烧蚀形貌. 结果表明，激光诱导等离子体及其产生的冲击波动力学均符合理想爆轰波理论，并且与靶材原子拓扑结构无关. 两种合金靶在纳秒激光烧蚀中均承受显著的过热并最终发生爆炸沸腾. 爆炸沸腾在靶表面形成一种多层级烧蚀形貌：由纳米孔洞广泛分布的微米凹坑. 相比于晶态靶，非晶合金靶呈现出较浅的凹坑以及较小的纳米孔洞. 这是由于非晶合金靶在激光烧蚀中具有较浅的热影响区，但过热程度较高. 进一步研究发现，这种微纳多层级烧蚀形貌可有效调节两种合金靶的表面润湿性能，从初始亲水性改变为疏水性；非晶和晶态靶的表面接触角分别提高约119%和64%. 本工作表明非晶合金对纳秒脉冲激光烧蚀具有更好的防护性能，并为非晶态或晶态合金的润湿性调节提供了一种可行且便捷的方法.